Progress In Electromagnetics Research, Vol. 131, 331–355, 2012

SLOT-LESS TORUS SOLID-ROTOR-RINGED LINE-START AXIAL-FLUX PERMANENT-MAGNET MOTOR

A. Mahmoudi[1, *], S. Kahourzade[1], N. A. Rahim[1], W. P. Hew[1], and N. F. Ershad[2]

[1]UM Power Energy Dedicated Advanced Centre (UMPEDAC), Wisma R&D UM, University of Malaya, Kuala Lumpur, Malaysia

[2]Electrical Engineering Department, Amirkabir University of Technology, Tehran, Iran

Abstract—This paper presents the design, analysis, and prototyping of a novel axial-flux permanent-magnet (AFPM) motor capable of auto-starting. The preliminary design is a slot-less double-sided solid-rotor line-start AFPM motor with 4 poles for high torque density and stable rotation. One spaced raised ring was added to the inner radii of the rotor disc for smooth line-start motor. The design allows the motor to operate at both starting and synchronous speeds. The basic equations for the solid ring of the rotor of the proposed axial-flux permanent-magnet motor are presented. Non-symmetry of the designed motor led to its 3D time-stepping finite element analysis (FEA) via ANSYS 13.0, which evaluated the design parameters and predicted the transient performance. The designed motor was fabricated and tested, the experimental results showing good agreement with FEA simulation results. The prototype motor showed high starting torque and good synchronization.

1. INTRODUCTION

Line-start permanent-magnet (LSPM) motors perform better than induction motors in applications that operate for a long period and require constant speeds (pumps, fans, compressors) [1]. For starting and operation, they can be connected directly to the utility supply. Their main advantages over induction machines are their higher efficiency, higher power factor, higher torque density, better thermal behavior, and lower sensitivity to frequency variations [2].

Received 3 July 2012, Accepted 29 August 2012, Scheduled 16 September 2012

* Corresponding author: Amin Mahmoudi (amaminmahmoudi@gmail.com).

Their starting and synchronization remain important challenges needing improvement, each depending on the motor and the load parameters [3].

Permanent-magnet machines generally can be axial-flux or radial-flux [4]. Advantages of axial-flux permanent-magnet (AFPM) motors over conventional radial-flux permanent-magnet (RFPM) motors include higher torque-to-weight ratio, good efficiency, adjustable air-gap, balanced rotor-stator attractive forces, and better heat-removal [5, 6]. Their air-gaps are planar and easily adjustable [7]. AFPM machine size and shape are a plus in limited-space applications, earning them their place in military and transport applications and motivating researchers to develop novel designs [8]. The starting and synchronization of LSPM motors have been the subject of much research, besides the effects of selected parameters on their performance [9–21]. In all these works, however, the focus has been on new methods for line-start radial-flux permanent-magnet (LSRFPM) motors while practically there is no publication on line-start axial-flux permanent-magnet (LSAFPM) motors.

Use of solid rotors instead of laminated rotors has advantages. The weakness and insufficient rigidness of the usual laminated rotor render it unsuitable for use in high-speed machines. A solid-rotor motor electromagnetically is weaker than a laminated rotor, though it is superior physically [22, 23]. At higher speeds, the solid-rotor-core can be used with mechanical bearings, because it easily maintains its balance. Also, research has shown that use of solid rotor in a poly-phase induction machine increases torque per ampere at standstill [24]. Moreover, high speeds and direct connection of load to the solid-rotor shaft do not affect the solid-rotor's ability to withstand the natural mechanical vibrations that threaten to damage the bearings.

AFPM machines can be single-sided or double-sided, with or without armature slots, with or without armature core, with internal or external permanent-magnet rotors, with surface-mounted or interior permanent-magnet, and single-stage or multi-stage machines [25]. Topologies of double-sided AFPM machines can be one-stator-two-rotor (TORUS) or two-stator-one-rotor (AFIR) [26]. This paper chooses the slot-less TORUS LSAFPM motor configuration for design, analysis, and prototyping. Leakage and mutual inductances in a slot-less motor are lower, and slot-due effects (flux ripple, cogging torque, and high-frequency rotor losses) are absent, making a low-noise machine [27]. With slot-less, too, the end windings are shorter, so copper losses reduce. The slot-less configuration has lower cogging torque, which makes for better synchronization.

The design and modeling of a solid-rotor-ringed line-start

axial-flux permanent-magnet motor that incorporates all the above mentioned benefits is hereby presented. It reports a successful design of an auto-start AFPM motor that at high speeds retains high efficiency and has sufficient starting ability when connected to the large loads. For auto-starting, a spaced and raised ring is added to the inner radii of the rotor disc that partially covers the inner yoke of the stator. The proposed design is novel, and the motor's structure unique. The interaction between the induced eddy-currents in the solid rotor rings and the rotating field in the air-gap between the rings and the inner end winding produces electromagnetic torque. In an AFPM motor, radial windings usually produce torque, whereas end windings usually are redundant, but in this work, inner end windings, too, produce torque.

The paper is organized as follows: Section 2 extracts the basic equations of the raised rotor-disc rings of the proposed axial-flux motor, Section 3 presents the structure, specifications and fabrication of the proposed LSAFPM motor, Section 4 includes the 3D finite element analysis of the proposed motor, Section 5 discusses the simulation and experimental results of the prototype motor, and Section 6 contains the conclusion.

2. FUNDAMENTAL DESIGN OF RAISED ROTOR-DISC RING

Presented are the details of the raised rings design at the inner radii of the rotor disc for the line-star axial-flux induction motor. The design aims to attain an appropriate solid-rotor-ringed axial-flux motor construction enabling the auto-start capability of the motor. The

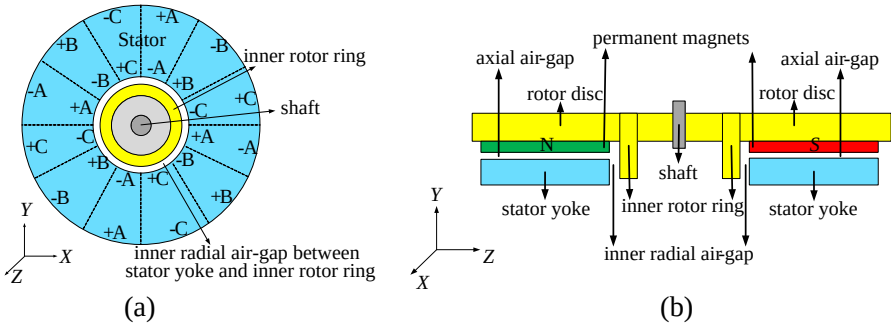

Figure 1. 2D views of the proposed designed motor, showing various parts of the motor including stator, rotor disc, rotor ring, air-gap, and winding configuration. (a) Radial view. (b) Axial view.

dimensioning is from the electromagnetic point of view only and hence the mechanical constraints are not considered. It is to be mention that the design procedure and parameter selection based on sizing equation and finite element method (FEM) for AFPM motor is not the subject of this work as it was presented in [8].

Figure 1 is a two-view cross-section of the proposed motor. Figures 1(a) and 1(b) are respectively the radial and the axial views. The winding configuration presented in Figure 1(a) is used for the designed motor. The analytical design of the rotor ring considered only the radial component of the flux density because it is what influences the motor's starting capability the most. Tangential tension $\sigma_{\tan}$ estimates the rotor-ring size for the desired torque production. Alternative to air-gap tangential tension, the magnitude of the internal power from the rotor volume of the induction machine defines the machine constant C [28]:

$$C = \frac{\pi^2}{\sqrt{2}} k_{w1} A B_{gr\_\max} \tag{1}$$

where A is the linear current density, $B_{gr\_\max}$ the radial air-gap maximum flux density, and k_{w1} the winding factor of the fundamental harmonic. The machine constant is written as a function of tangential tension [28]:

$$C = \sqrt{2}\sigma_{\tan}\pi^2 k_{w1} \tag{2}$$

From Equations (1) and (2), the tangential tension is:

$$\sigma_{\tan} = \frac{A B_{gr\_\max}}{2} \tag{3}$$

The tangential tension in the air-gap can be calculated from:

$$\sigma_{\tan} = \frac{\tau}{R_{ave} S_r} \tag{4}$$

where R_{ave} is the mean value of the rotor ring's inner and outer radii, S_r the rotor ring's surface facing the air-gap between the rotor ring and the stator surface, and τ the torque. The tangential force $F_{\tan}$ is:

$$F_{\tan} = \sigma_{\tan} S_r \tag{5}$$

The radial air-gap length between the rotor ring and the stator yoke surface should be selected with great care. Increased air-gap length increases the stator's copper losses and decreases the rotor's eddy current losses. Loss is minimum between the rising copper losses and the rotor's diminishing harmonic eddy current. The highest possible air-gap flux density ensures the attainment of a high-performing maximum-torque solid-rotor-ringed LSAFPM motor.

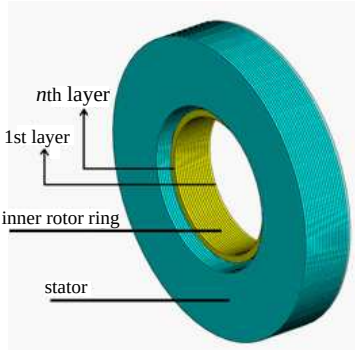

Figure 2. Division of the rotor ring and stator into n parallel active regions.

For acceptable calculation results of the analytical design, the rotor ring and the stator were divided into a number of parallel active circular sub-volumes as shown in Figure 2. By this, the curvature of the machine is assumed to have no further effect on the performance of an individual sub-machine. Densities of the rotor and the stator fluxes were studied in each area from 1 to n. Upon selection of the rotor ring slot width b_r and rotor ring slot pitch $\tau_r(1 \ldots n)$, the motor's inner parts must not be allowed to saturate. The flux density of the rotor-ring teeth is calculated from [29]:

$$B_{dr(1\ldots n)} = \frac{B_{gr\_\max}\tau_{r(1\ldots n)}}{\tau_{r(1\ldots n)} - b_r} \tag{6}$$

The allowable rotor ring tooth flux density B_{dr} of radial-flux induction machines is between 1.5 T and 2.2 T [29] (this range is also used here). Assuming the total flux of the slot pitch to flow along the teeth, no flux in either the slots or their insulation, and non-saturated motor teeth, allows calculation of the rotor-ring teeth length as:

$$w_{dr} = \frac{\tau_{r(n)}B_{gr\_\max}}{B_{dr(n)}} \tag{7}$$

Thickness of the rotor ring is:

$$w_{th\_r} = \frac{\phi_{rr}}{2B_{rr}k_{rFe}l_e} \tag{8}$$

where B_{rr} is the peak flux density of the rotor ring, k_{rFe} the space coefficient of the iron (which depends on the relative thickness of the electric sheet insulation to the press fit of the stack), l_e the equivalent rotor ring core length, and ϕ_{rr} the peak value of the main radial flux

penetrating the rotor ring and the stator winding. The rotor yoke flux density allowable for radial-flux induction motor is 0.4 T to 1.6 T [29] (this range is also used here). The mechanical strength of a solid rotor ring is reliable, unlike that of a laminated rotor whose minimum thickness may only be determined by mechanical constraints.

The length of the coil l_m depends on the number of pole-pairs p, the stator core length l_{ea}, the pole pitch τ_p, the chord factor χ (the ratio of the coil span W to the pole pitch τ_p), and the stator core thickness l_{er}:

$$l_m = p\left(2l_{ea} + \chi\tau_{p\_in} + \chi\tau_{p\_out} + 2l_{er}\right) \tag{9}$$

τ_{p_in} and τ_{p_in} are the pole pitches at inner and outer radius respectively. In rotor ring design of the LSAFPM motor, the radial windings which produce torque in the synchronous state are considered as the end windings of the axial windings during the starting period. The currents flowing into the radial windings produce end-winding leakage flux. Due to the difficulty of analysing the geometry of the windings in axial-flux machines and because the leakage flux is influenced by all the phases of poly-phase machines, the inductance factors λ_E and λ_W are determined empirically. Richter provided calculated values of the inductance factors valid for induction machines [30]. The end-winding leakage inductances L_{WS} in the inner (L_{WS_in}) and the outer (L_{WS_out}) circumferences of the proposed axial-flux induction machine are:

$$L_{WS\_in} = \frac{4m}{Q} q \cdot N_{ph}^2 \cdot \pi \cdot f \cdot \mu_0 \left(2 \cdot l_{er} \cdot \lambda_E + \chi \cdot \tau_{p\_in} \cdot \lambda_W\right) \tag{10}$$

$$L_{WS\_out} = \frac{4m}{Q} q \cdot N_{ph}^2 \cdot \pi \cdot f \cdot \mu_0 \left(2 \cdot l_{er} \cdot \lambda_E + \chi \cdot \tau_{p\_out} \cdot \lambda_W\right) \tag{11}$$

where m is the number of phases, N_{ph} is the number of winding turns per phase, f the frequency, Q the number of slots, q the number of slots per pole and per phase, τ_{p_in} the pole pitch at inner radius, τ_{p_out} the pole pitch at outer radius, and μ_0 the permeability of free space.

3. MACHINE STRUCTURE

The designed motor is an inside-out double-rotor single-stator LSAFPM motor (see Figure 3 for an exploded view). Table 1 lists the motor's dimensions and specifications.

To build the stator, silicon-iron paper with a thickness of 0.1 mm was used for lamination. The axial flux motor's stator is either laminated spirally or axially. As shown in Figure 4(a), in this work spiral configuration was implemented. Also, a simple 3-phase winding

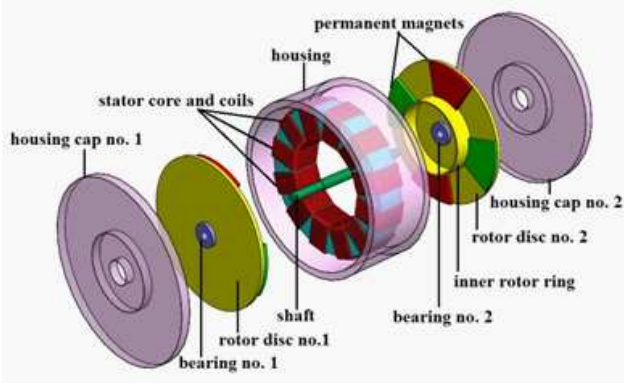

Figure 3. Exploded diagram of the proposed LSAFPM motor.

Table 1. The motor's dimensions and specifications.

rated voltage (line-line RMS)	V_r	18 V
rated power	P_r	250 W
rated torque	τ_r	15 Nm
number of poles	p	4
number of phases	m	3
drive frequency	f	50 Hz
stator outer diameter	D_{so}	21 mm
stator inner diameter	D_{si}	120 mm
ratio of inner diameter to outer diameter of stator	λ	0.57
rotor ring outer diameter	D_{ro}	112 mm
rotor ring inner diameter	D_{ri}	102 mm
rotor ring axial length	L_r	10 mm
magnet's axial length	L_{pm}	4 mm
pole pitch	γ_p	100°
stator-yoke thickness + winding thickness	$L_{cs} + l_w$	36 + 4 mm
rotor-yoke thickness	L_{cr}	6 mm
number of winding turns per phase	N_{ph}	4×90
axial air-gap flux density	B_{ga}	0.3 T
axial air-gap length	g_a	2 mm
radial air-gap length	g_r	2 mm

(a) (b)

Figure 4. The stator of the prototype line-start axial-flux permanent-magnet motor. (a) Spiral laminated stator. (b) Stator winding is made of 12 coils with 90 turns each.

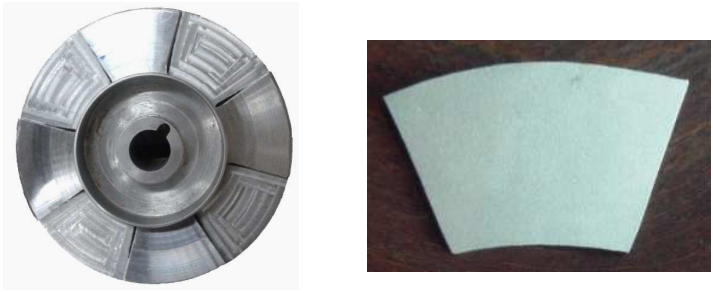

(a) (b)

Figure 5. The prototype line-start axial-flux permanent-magnet motor's rotor structure and its trapezoidal NdFeB permanent magnet. (a) Rotor. (b) Trapezoidal NdFeB permanent magnet.

with star connection was adopted as stator winding (Figure 4(b)). The details of winding configuration were presented in Figure 1(a). To fix the windings into place, prevent it from vibration during motor operation and to increase its insulation capability, a type of resin was applied, giving the windings characteristics such as stiffness in working temperature and good thermal conductivity for heat-release.

Figure 5 shows the motor's rotor and its permanent magnets geometry. Figure 5(a) is the single disc of the rotor which was constructed from mild-steel with its inner ring enabling starting capability of the motor. In each rotor disc, 4 axially-magnetized Nd-Fe-B permanent magnets shown in Figure 5(b) are mounted on the disc surface facing the stator. The permanent magnets used in the machine prototype have 1.3 T remanence and 900 kA/m demagnetizing field.

4. FINITE ELEMENT ANALYSIS

The governing equations for the FEA are [31]:

$$\nabla \times \vec{B} = \mu \vec{J} \tag{12}$$

$$\nabla \times \vec{J} = -\sigma \frac{d\vec{B}}{dt} \tag{13}$$

$$\vec{B} = \nabla \times \vec{\psi} \tag{14}$$

where $\vec{B}$, $\vec{J}$, $\vec{\psi}$, σ, and μ are respectively the magnetic flux density, the current density, the magnetic vector potential, the electrical conductivity, and the magnetic permeability.

Considering $\vec{H}$ as the magnetic field intensity, the above mentioned Equations (12)–(14) lead to the following equation:

$$\nabla \times \left(\frac{1}{\sigma} \nabla \times \vec{H} \right) + \frac{\partial \vec{B}}{\partial T} = 0 \tag{15}$$

The result is a formula whose vector fields are represented by first-order edge elements and scalar fields by second-order nodal unknowns. The circuit equation during motoring is given by:

$$u = R_{ph} i + L_e \frac{di}{dt} + e \tag{16}$$

$$e = \frac{l}{s} \iint\limits_{\Omega_e} \frac{\partial \vec{\psi}}{\partial T} d\vec{\Omega} \tag{17}$$

where u is the applied source voltage, R_{ph} the winding resistance per phase, L_e the end winding inductance per phase, e the electromotive force (EMF) per phase, i the phase current, l the radial length of iron core, S the conductor area of each turn of phase winding, and Ω_e the total cross-sectional area of conductors of each phase winding.

The motion of the machine is given by:

$$T_{em} - T_L - C_v \omega_r = j_m \frac{d\omega_r}{dt} \tag{18}$$

where, j_m is the rotor momentum of inertia, ω_r the rotor speed, T_L the load torque, T_{em} the electromagnetic torque, and C_v the damping coefficient.

Therefore, after discretization, the above mentioned three types of equations can be solved at each time step. Consequently both steady-state and transient performances of the proposed machine can be calculated. The proposed LSAFPM motor has a unique construction; its lack of symmetry makes 3D-FEA a design requisite. Note that

3D-FEM facilitates field analysis of electromagnetic problems with complex geometries. The model's complex magnetic circuit was analysed for an overall view of the saturation levels in various parts of the motor, and to extract the motor's characteristics. An advantage of 3D-FEA is that various components of flux density can be calculated highly accurately [32–40]. The design was simulated on commercial ANSYS 13.0 software [41]. Corresponding materials and circuit currents were assigned to each model segment. Figure 6 shows the FEA structure of designed LSAFPM motor, which is a 3D auto-mesh: tetrahedral elements with 6 nodes fitting the circular shape of the layers starting from the inner to the outer diameter of the motor. Figure 6(a) includes the entire structure of the motor while Figure 6(b) only includes the rotors and the permanent magnets.

Evaluation of the magnetic flux density is important because the

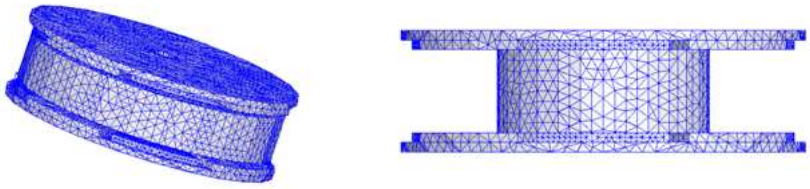

Figure 6. The proposed line-start axial-flux permanent-magnet motor 3D auto-mesh: tetrahedral elements generated on ANSYS software. (a) The entire structure of the motor indicating the stator between the rotors. (b) Solid rotor iron and permanent-magnet poles.

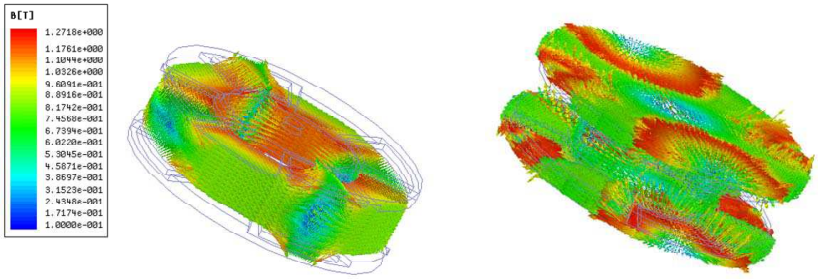

Figure 7. Field analysis of the proposed LSAFPM motor, in ANSYS 13.0. (a) Flux-density contour in stator. (b) Flux density contour in the rotors.

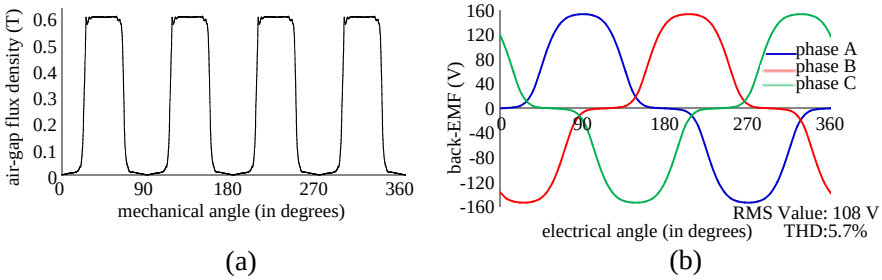

Figure 8. Distribution of air-gap magnetic flux density in average radius versus mechanical angle and back-EMF at synchronous speed (1500 rpm). (a) Air-gap magnetic flux density. (b) Back-EMF.

flux density saturation of the stator or the rotor affects the motor performance and reduces the efficiency. Figure 7 depicts the post-synchronization magnetic flux density distribution in various sectors of the designed LSAFPM motor. Figure 7(a) is the flux density plot in the stator showing higher flux density at the inner yoke of the stator due to condenser winding in those areas. Figure 7(b) is the flux density plot in the rotor disc and the inner rotor ring showing higher flux density around the permanent magnets and the lowest flux density on the rotor ring.

Figure 8 shows the magnetic flux density and back EMF of the motor. Figure 8(a) is the air-gap flux density distribution, in average radius. The maximum flux density is obviously 0.6 T, averaging 0.3 T. Due to the slot-less type AFPM motor, air-gap magnetic field distribution is smooth, and consequently the variation of back-EMF is also smooth and almost sinusoidal. Figure 8(b) shows the no-load back EMF at rated speed (1500 rpm), beside the FEA-calculated THD and back-EMF RMS. It should be noted that the optimization of the designed motor is not the subject of this paper.

5. RESULTS AND DISCUSSION

Figure 9 gives a schematic view of the *d-q* equivalent circuits of the proposed LSAFPM motor. The LSAFPM motor starts as an induction motor by the resultant of two torque components, i.e., cage torque and magnet opponent torque (braking torque). When the motor approaches synchronous speed, synchronization begins and its operation becomes synchronous. No eddy current except harmonic field current then flows into the solid rotor-ring.

In synchronous state, two torque components (reluctance torque

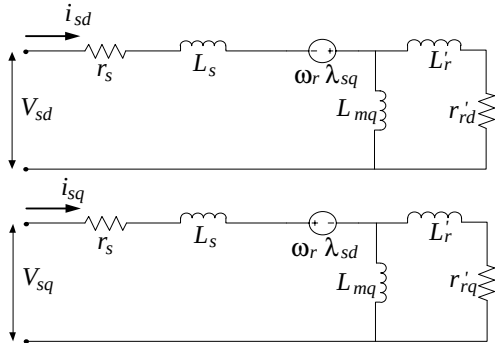

Figure 9. A *d-q* reference frame equivalent circuit of proposed LSAFPM motor.

and synchronous torque) mobilize the rotor. [42] describes the dynamic performance of line-start permanent-magnet motors in a stationary *d-q* reference frame:

$$V_{sq} = r_s i_{sq} + \omega_r \lambda_{sd} + \frac{d\lambda_{sq}}{dt} \tag{19}$$

$$V_{sd} = r_s i_{sd} - \omega_r \lambda_{sq} + \frac{d\lambda_{sd}}{dt} \tag{20}$$

$$V'_{rq} = r'_{rq} i'_{rq} + \frac{d\lambda'_{rq}}{dt} = 0 \tag{21}$$

$$V'_{rd} = r'_{rd} i'_{rd} + \frac{d\lambda'_{rd}}{dt} = 0 \tag{22}$$

where V_{sq}, V_{sd}, V'_{rq}, and V'_{rd} are the stator voltages and the rotor voltages referred to stator, λ_{sq}, λ_{sd}, λ'_{rq}, and λ'_{rd} the stator linkage fluxes and the rotor linkage fluxes, and i_{sq}, i_{sd}, i'_{sq}, and i'_{sd} the stator currents and the rotor currents, ω_r, r_s, r'_{rd}, and r'_{rq} respectively the rotor speed, stator resistance, and rotor resistances (all relative to the stator). The stator linkage flux and the rotor linkage flux are:

$$\lambda_{sq} = L_{sq} i_{sq} + L_{mq} i'_{rq} \tag{23}$$

$$\lambda_{sd} = L_{sd} i_{sd} + L_{md} i'_{rd} + \lambda'_m \tag{24}$$

$$\lambda'_{rq} = L'_{rq} i'_{rq} + L_{mq} i_{sq} \tag{25}$$

$$\lambda'_{rd} = L'_{rd} i'_{rd} + L_{md} i_{sd} + \lambda'_m \tag{26}$$

where L_{sq}, L_{sd}, L'_{rq}, L'_{rd} are the stator self-inductances and the rotor self-inductances, L_{mq} and L_{md} the mutual inductances, and λ'_m the

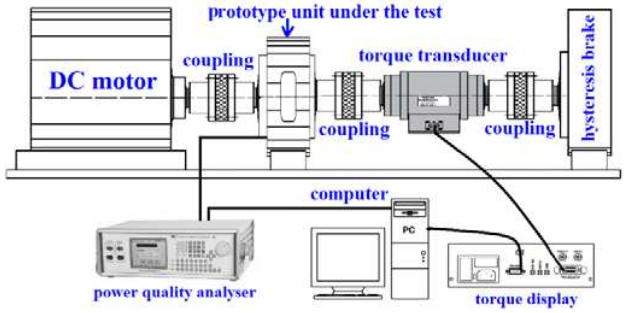

Figure 10. Hardware schematic for experimental tests of prototype LSAFPM motor.

permanent-magnet flux. The electromagnetic torque is then:

$$T_{em} = \frac{3p}{2}(L_{sd} - L_{sq})i_{sd}i_{sq} + \frac{3p}{2}(L_{md}i'_{rd}i_{sq} - L_{mq}i'_{rq}i_{sd}) + \frac{3p}{2}\lambda'_m i_{sq} \quad (27)$$

with the first term being the reluctance torque, the second term the cage torque, and the third term the magnet's synchronous torque.

In order to test the performance of the prototype motor, an experimental setup was built. The hardware schematic for the experimental setup is shown in Figure 10. Since the speed in not very high, in-line torque transducer with suspended installation and single-element coupling to create shorter drive train were used. Hysteresis brake on the motor shaft provides the desired torque load. Back-EMF and speed/time response were the main performance parameters to obtain. It should be noted that during cruising-speed test, secondary measurement such as temperature rise in the motor's critical sections were also monitored.

To analyze the proposed model in transient state during auto-starting, the motor was run as an induction motor (i.e., without any permanent magnets) with the aid of FEA. The stator was excited via a three-phase voltage supply; the motor then began rotating as an induction motor and at sub-synchronous speeds. Field equations were coupled with circuit equations for conductors, because in transient simulations, supply voltages are applied and currents are unknown. Classical Newton-Raphson algorithm was used for the nonlinearities. A major difficulty for transient simulation is that induced currents on the rotor rings must be calculated in each step before calculating the torque.

Line-start synchronous motor is a low-cost solution that works reasonably well if the motor load and power supply voltage remains mostly constant. The prototyped motor was also tested in transient

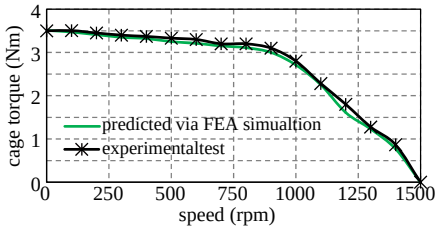

Figure 11. Experimental and FEA predicted induced induction torque of proposed LSAFPM motor.

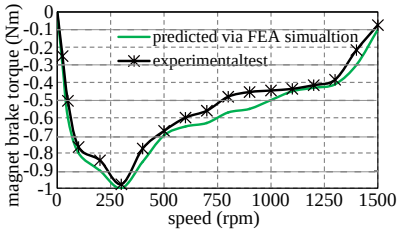

Figure 12. Experimental and FEA predicted braking torque caused by permanent magnets during start up.

state during auto-starting without permanent magnet, just like an induction motor. The performance comparison of the experimental results versus the FEA simulations agrees well. Figure 11 gives the proposed motor induced-torque curves both experimentally and via simulation. It should be noted that the torque-speed characteristic of this type of motor does not follow the typical torque-speed characteristic of radial induction motors. It is clearly seen that the torque reduces smoothly from its maximum value at the speed of zero and reaches to zero at the synchronous speed.

The starting and the synchronizing of LSAFPM motors are challenging feats, primarily due to the brake torque of the magnet poles. Figure 12 shows the permanent-magnet braking torque calculated via FEA and experimentally for the proposed LSAFPM motor. This torque is developed between starting and synchronous speed. It reaches the maximum value at low speed. It is then reduced and finally reaches to a constant value at synchronous speed. For the initial period, the permanent magnet brake toque is negative, which causes vibration and noise during starting period of the LSAFPM motor. This phenomenon of oscillatory torques during the run-up period needs serious attention from the designers and users of the LSAFPM motors. The magnet braking torque T_b is given by [43]:

$$T_b = \frac{3pr_s(1-s)E_0^2}{2\omega_s} \times \frac{r_s^2 + X_{sq}^2(1-s)^2}{(r_s^2 + X_{sd}X_{sq}(1-s)^2)} \tag{28}$$

with E_0, X_{sd}, X_{sq}, ω_s, and s respectively being the magnet back-EMF, the d-axis stator reactance, the q-axis stator reactance, the synchronous speed, and the slip. This torque resists the cage torque that may cause failures in starting or synchronizing.

It is well known that a key factor in the working of line-start permanent-magnet motors is the starting performance. Interaction

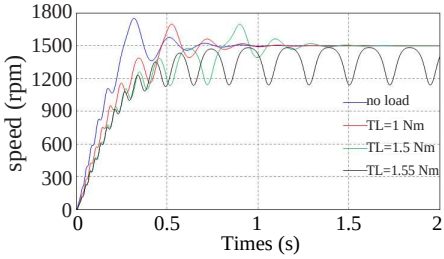

Figure 13. Simulation results of the LSAFPM motor run-up speed response under various load torques.

between the eddy-currents in the solid-steel rotor ring and the rotating field in the air-gap between the ring and the end winding produces electromagnetic torque. Simulation based speed-time responses of the designed LSAFPM motor under various load inertia are shown in Figure 13. In line-start motors, the load inertia clearly matters to synchronization: the higher the inertia, the more difficult it is to synchronize. The motors were started at no-load condition. The rotor momentum inertia of $j_m = 0.2\,\text{Nm}$ was used during the simulations for comparison with the experimental results. The motor easily synchronizes, especially considering the capabilities of the starting torque.

The synchronization time increases to 1.1 sec for the load inertia of 1 Nm from 0.9 sec for the no-load condition. A noteworthy result is the maximum load torque that the motor can handle, which is clearly limited to 1.5 Nm. At 1.55 Nm load torque, the motor failed to synchronize and started to oscillate between 1140 rpm and 1480 rpm. Figure 14 shows the corresponding electromagnetic torque and input current versus time curves, for the load torques mentioned. It is evident that electromagnetic torque oscillates during run-up time and finally settles down at the value of the load torque in synchronous speed. The maximum current value during initial period reaches 5 to 6 times of its maximum value during synchronization. Figures 14(g) and 14(h) show that for the TL = 1.55 Nm load torque, both electromagnetic torque and input current never stop oscillation.

The back-EMF of the fabricated motor in various speeds was measured in open-circuit test. Figure 15 shows the voltage and its harmonic spectrum obtained experimentally in open-circuit test at rated speed. The finite element analysis simulation and experimental results comparison are tabulated in Table 2. Experimental results almost agree with those of simulation.

Figure 16 shows the measured starting and synchronizing

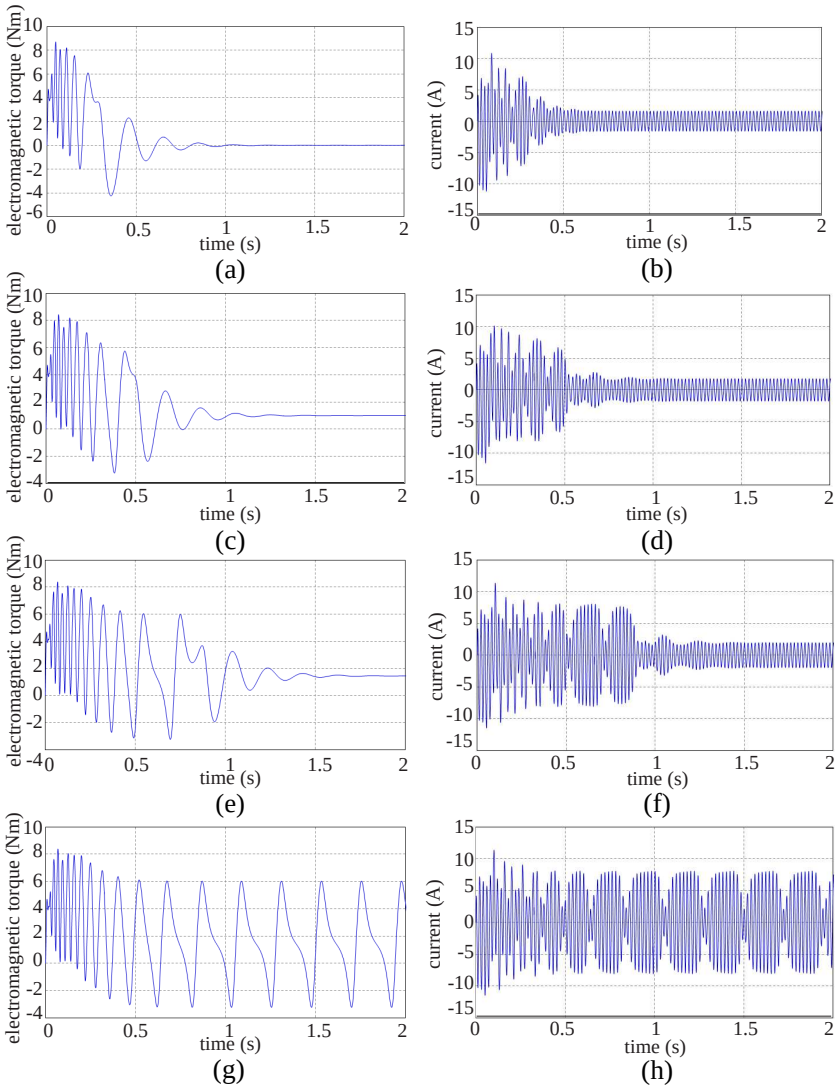

Figure 14. Torque and current versus time responses of the designed LSAFPM motor under various load torques. (a) Torque versus time response (no-load). (b) Current versus time response (no-load). (c) Torque versus time response ($T_L = 1\,\text{Nm}$). (d) Current versus time response ($T_L = 1\,\text{Nm}$). (e) Torque versus time response ($J_L = 1.5\,\text{Nm}$). (f) Current versus time response ($J_L = 1.5\,\text{Nm}$). (g) Torque versus time response ($T_L = 1.55\,\text{Nm}$). (h) Current versus time response ($T_L = 1.55\,\text{Nm}$).

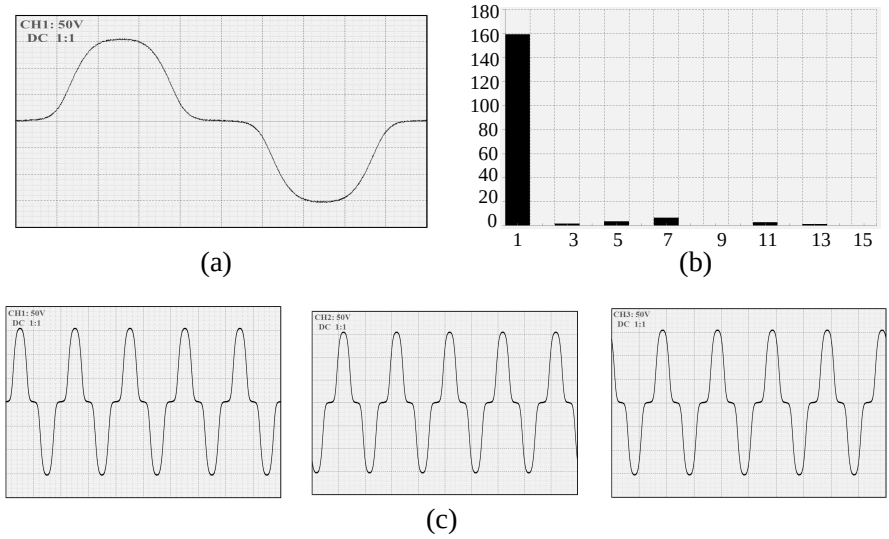

Figure 15. Voltage and its harmonic spectrum obtained experimentally from open circuit test. (a) Oscilloscope trace of back-EMF waveform (time scale: 20 ms/div; voltage scale: 50 V/div). (b) Back-EMF harmonic spectrum (total harmonic distortion is 5.7%). (c) Oscilloscope trace of three-phase back-EMF (5 cycles).

Table 2. Back-EMF comparison between experimental and FEA results.

Back-EMF		$V_{\max}$	V_{RMS}	THD %
1500 rpm	experimental	153.5	108.5	5.7
	FEA	153	108	5.7
750 rpm	experimental	73.2	51.7	5.9
	FEA	52.5	51.1	5.8

performance of the prototype machine together with the simulated results from FEA. It is clear that the prototype line-start AFPM motor started the 1.3 Nm load, accelerated to the synchronous speed and finally locked-in and synchronized to supply line frequency (1500 rpm). The oscillatory nature of the speed response is due to the interaction between the rotor magnets and the stator supply current. The figure also shows a validation of the accuracy of the simulation results for the prototype LSAFPM motor.

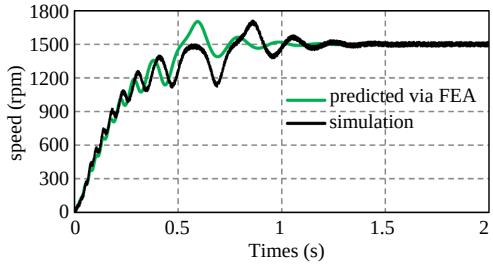

Figure 16. Experimental and predicted speed/time response of prototype motor under 1.3 Nm load.

6. CONCLUSION

This paper reported the design process, finite element analysis, and prototyping of a solid-rotor-ringed LSAFPM motor as a novel structure for the AFPM motor. A unique rotor comprised of a spaced raised solid ring that enables smooth line-start of the proposed motor was presented and its relevant equations were extracted. The steady-state and transient performance of the proposed design motor was examined via 3D finite element analysis. The motor was fabricated and tested. The experimental results of dynamic starting and synchronization performance from prototype motor agreed with those of simulation results. The paper verifies successful design of a 1/3hP 4-pole auto-start slot-less inside-out axial-flux permanent-magnet motor, its good synchronization at rated speed, and its sufficient starting torque when connected to a maximum load torque of 1.5 Nm. Among the advantages of the solid-rotor motor are its physical ability to withstand natural vibrations that make it suitable for high-speed applications and increased torque per ampere at standstill.

Nomenclature

A: linear current density
$\vec{B}$: magnetic flux density
B_{dr}: rotor ring tooth flux density
B_{ga}: axial air-gap flux density
$B_{gr\_\max}$: radial air-gap maximum flux density
b_r: rotor ring slot width
B_{rr}: peak flux density of rotor ring
C: machine constant

C_v: damping coefficient
D_{so}: stator outer diameter
D_{si}: stator inner diameter
D_{ro}: rotor-ring outer diameter
D_{ri}: rotor-ring inner diameter
E_0: magnet back-EMF
e: electromotive force (EMF) per phase
f: frequency
$F_{\tan}$: tangential force
g_a: axial air-gap length
g_r: radial air-gap length
$\vec{H}$: magnetic field intensity
i_{sd}: d-axis component of stator current
i_{sq}: q-axis component of stator current
i'_{rd}: d-axis component of rotor current referred to stator
i'_{rq}: q-axis component of rotor current referred to stator
$\vec{J}$: current density
j_m: rotor moment of inertia
j_L: load inertia
i: phase current
k_{W1}: winding factor of fundamental harmonic
k_{rFe}: space factor of the iron
L_{cr}: rotor-yoke thickness
L_{cs}: stator-yoke thickness
L_e: end winding inductance per phase
l: radial length of iron core
l_e: equivalent rotor ring core length
l_{ea}: equivalent stator core length
l_{er}: equivalent stator core thickness
l_m: length of one turn of the winding
L_{sd}: d-axis component of stator self-inductance
L_{sq}: q-axis component of stator self-inductance
L'_{rd}: d-axis component of rotor self-inductance
L'_{rq}: q-axis component of rotor self-inductance
L_{md}: d-axis component of stator mutual-inductance

L_{mq}: q-axis component of stator mutual-inductance
L_{pm}: magnet's axial length
L_r: rotor ring axial length
L_{WS}: end winding leakage inductances
L_{SW_in}: end winding leakage inductances at inner radius
L_{SW_out}: end winding leakage inductances at outer radius
l_w: winding thickness
m: number of phases
n: number of concentric circular divisions for rotor ring and stator
N_{ph}: number of winding turns per phase
p: number of pole pairs
P_r: rated power
Q: number of slots
q: number of slots per pole per phase
R_{ave}: average inner and outer radii of rotor ring
R_{ph}: winding resistance per phase
r_s: stator resistance
r'_{rd}: d-axis component of rotor resistances referred to stator
r'_{rq}: q-axis component of rotor resistances referred to stator
S: conductor area of each turn of phase-winding
s: slip
S_r: rotor ring's surface facing the air-gap between rotor ring and stator surface
T_b: magnet breaking torque
T_{em}: electromagnetic torque
T_L: load torque
T_r: rated torque
u: applied source voltage
V_{sd}: d-axis component of stator voltage
V_{sq}: q-axis component of stator voltage
V'_{rd}: d-axis component of rotor voltage referred to stator
V'_{rq}: q-axis component of rotor voltage referred to stator
V_r: rated voltage
W: coil span
w_{dr}: length of rotor-ring teeth

w_{th_r}: thickness of the rotor ring
X_{sd},: d-axis stator reactance
X_{sq}: q-axis stator reactance
γ_p: pole pitch
λ: ratio of inner diameter to outer diameter of stator
λ_{sd}: d-axis component of stator flux linkage
λ_{sq}: q-axis component of stator flux linkage
λ'_{rd}: d-axis component of rotor flux linkage
λ'_{rq}: q-axis component of rotor flux linkage
λ'_m: permanent magnet flux
λ_E: empirical inductance factor
λ_W: empirical inductance factor
μ: magnetic permeability
μ_0: permeability of free space
σ: electrical conductivity
$\sigma_{\tan}$: tangential tension
τ: torque
τ_p: pole pitch
τ_{p_in}: pole pitch at inner radius
τ_{p_out}: pole pitch at outer radius
$\tau_{r(1\ldots n)}$: rotor ring slot pitch
$\vec{\psi}$: magnetic vector potential
ϕ_{rr}: peak value for the main radial flux penetrating the rotor ring and the stator winding
χ: chord factor
Ω_e: total cross-sectional area of conductors per phase
ω_r: rotor speed
ω_s: synchronous speed

ACKNOWLEDGMENT

The authors acknowledge the University of Malaya's provision of the High Impact Research Grant No. D000022-16001 funding the Hybrid Solar Energy Research Suitable for Rural Electrification.

REFERENCES

1. Fei, W., P. Luk, J. Ma, J. X. Shen, and G. Yang, "A high-performance line-start permanent magnet synchronous motor amended from a small industrial three-phase induction motor," *IEEE Trans. Magn.*, Vol. 45, No. 10, 4724–4727, Oct. 2009.
2. Knight, A. M. and C. I. McClay, "The design of high-efficiency line-start motors," *IEEE Trans. Ind. Appl.*, Vol. 36, No. 36, 1555–1562, Nov./Dec. 2000.
3. Aliabad, A. D., M. Mirsalim, and N. F. Ershad, "Line-start permanent-magnet motors: Significant improvements in starting torque, synchronization, and steady-state performance," *IEEE Trans. Magn.*, Vol. 46, No. 12, 4066–4072, Dec. 2010.
4. Cavagnino, A., M. Lazzari, F. Profumo, and A. Tenconi, "A comparison between the axial flux and the radial flux structures for PM synchronous motors," *IEEE Trans. Ind. Appl.*, Vol. 38, No. 6, 1517–1524, Nov./Dec. 2002.
5. Mirimani, S. M., A. Vahedi, and F. Marignetti, "Effect of inclined static eccentricity fault in single stator-single rotor axial flux permanent magnet machines," *IEEE Trans. Magn.,* Vol. 48, No. 1, 143–149, Jan. 2012.
6. De la Barriere, O., S. Hlioui, H. Ben Ahmed, M. Gabsi, and M. LoBue, "3-D formal resolution of Maxwell equations for the computation of the no-load flux in an axial flux permanent-magnet synchronous machine," *IEEE Trans. Magn.,* Vol. 48, No. 1, 128–136, Jan. 2012.
7. De Donato, G., F. G. Capponi, and F. Caricchi, "No-load performance of axial flux permanent magnet machines mounting magnetic wedges," *IEEE Trans. Ind. Electron.*, Vol. 59, No. 10, 3768–3779, Oct. 2012.
8. Mahmoudi, A., N. A. Rahim, and W. P. Hew, "Axial-flux permanent-magnet motor design for electric vehicle direct drive using sizing equation and finite element analysis," *Progress In Electromagnetics Research*, Vol. 122, 467–496, 2012.
9. Ding, T., N. Takorabet, F. M. Sargos, and X. Wang, "Design and analysis of different line-start PM synchronous motors for oil-pump applications," *IEEE Trans. Magn.*, Vol. 45, No. 3, 1816–1819, Mar. 2009.
10. Honsinger, V. B., "Permanent magnet machines: Asychronous operation," *IEEE Trans. Power Apparatus and Systems*, Vol. 99, No. 4, 1503–1509, Jul. 1980.
11. Kim, B. T. and B. I. Kwon, "Influence of space harmonics

on starting performance of a single-phase line start permanent-magnet motor," *IEEE Trans. Magn.*, Vol. 44, No. 22, 4668–4672, Dec. 2008.

12. Marcic, T., B. Stumberger, G. Stumberger, M. Hadziselimovic, P. Virtic, and D. Dolinar, "Line-starting three-and single-phase interior permanent magnet synchronous motors-direct comparison to induction motors," *IEEE Trans. Magn.*, Vol. 44, No. 11, 4413–4416, Nov. 2008.
13. Miller, T. J. E., "Synchronization of line-start permanent-magnet ac motors," *IEEE Trans. Power Apparatus and Systems*, Vol. 103, No. 7, 1822–1828, Jul. 1984.
14. Peralta-Sánchez, E. and A. Smith, "Line-start permanent-magnet machines using a canned rotor," *IEEE Trans. Ind. Appl.*, Vol. 45, No. 3, 903–910, May/Jun. 2009.
15. Isfahani, A. H. and S. Vaez-Zadeh, "Effects of magnetizing inductance on start-up and synchronization of line-start permanent-magnet synchronous motors," *IEEE Trans. Magn.*, Vol. 47, No. 4, 823–829, Apr. 2011.
16. Peralta-Sanchez, E., A. C. Smith, and J. J. Rodriguez-Rivas, "Steady-state analysis of a canned line-start PM motor," *IEEE Trans. Magn.*, Vol. 47, No. 10, 4080–4083, Oct. 2011.
17. Lee, B.-H., J.-P. Hong, and J.-H. Lee, "Optimum design criteria for maximum torque and efficiency of a line-start permanent-magnet motor using response surface methodology and finite element method," *IEEE Trans. Magn.*, Vol. 48, No. 2, 863–866, Feb. 2012.
18. Rahman, M. A., A. M. Osheiba, K. Kurihara, M. A. Jabbar, W. P. Hew, W. Kai, and H. M. Zubayer, "Advances on single-phase line-start high efficiency interior permanent magnet motors," *IEEE Trans. Ind. Elect.,* Vol. 59, No. 3, 1333–1345, Mar. 2012.
19. Aliabad, A. D. and M. Mirsalim, "Analytic modelling and dynamic analysis of pole-changing line-start permanent-magnet motors," *IET Elect. Power Appl.*, Vol. 6, No. 3, 149–155, Mar. 2012.
20. Baek, S. W. and B. I. Kwon, "Optimum design of a single-phase line-start PM motor considering efficiency, maximum torque, and starting torque," *IEEE Trans. Magn.*, Vol. PP, No. 99, 1, May 2012.
21. Baek, S. W., B. I. Kim, and B. I. Kwon, "Practical optimum design based on magnetic balance and copper loss minimization for a single-phase line start PM motor," *IEEE Trans. Magn.*, Vol. 47,

No. 10, 3008–3011, Oct. 2011.

22. Sarma, M., "Current-density distribution in solid-rotor induction motor," *IEEE Trans. Magn.*, Vol. 15, No. 6, 1473–1475, Nov. 1979.
23. Sarma, M. S. and G. R. Soni, "Solid-rotor and composite-rotor induction Machines," *IEEE Trans. Aerospace and Electronic Systems*, Vol. 8, No. 2, 147–155, Mar. 1972.
24. Wilson, J. C., E. A. Erdelyi, and R. E. Hopkins, "Aerospace composite-rotor induction motors," *IEEE Trans. Aerospace and Electronic Systems*, Vol. 3, No. 2, 18–23, Jun. 1965.
25. Gieras, J. F., R. Wang, and M. J. Kamper, *Axial Flux Permanent Magnet Brushless Machines*, 2nd Edition, Springer-Verlag, New York, 2008.
26. Mahmoudi, A., N. A. Rahim, and W. P. Hew, "A comparison between the TORUS and AFIR axial-flux permanent-magnet machine using finite element analysis," *IEEE International Electric Machine and Drives Conference (IEMDC),* 242–247, May 2011.
27. Mahmoudi, A., S. Kahourzade, N. A. Rahim, and H. W. Ping, "Improvement to performance of solid-rotor-ringed line-start axial-flux permanent-magnet motor," *Progress In Electromagnetics Research*, Vol. 124, 383–404, 2012.
28. Müller, G., K. Vogt, and B. Ponick, *Berechnung Elektrischer Maschinen*, Wiley-VCH, Weinheim, 2008.
29. Vogt, K. and G. Muller, *Elektrische Maschinen Berechnung Rotierender Elektrischer Maschinen*, Veb Verlag Technik, Berlin, 1988.
30. Richter, R. and R. Brüderlink, *Elektrische Maschinen: Die Induktionsmachinen*, 4th Edition, Birkhäuser Verlag, Basel, 1954.
31. Bianchi, N., *Electrical Machine Analysis Using Finite Element*, Taylor & Francis, CRC Press, 2005.
32. Vaseghi, B., N. Takorabet, and F. Meibody-Tabar, "Transient finite element analysis of induction machines with stator winding turn fault," *Progress In Electromagnetics Research*, Vol. 95, 1–18, 2009.
33. Torkaman, H. and E. Afjei, "FEM analysis of angular misalignment fault in SRM magnetostatic characteristics," *Progress In Electromagnetics Research*, Vol. 104, 31–48, 2010.
34. Touati, S., R. Ibtiouen, O. Touhami, and A. Djerdir, "Experimental investigation and optimization of permanent magnet motor based on coupling boundary element method with permeances network," *Progress In Electromagnetics Research*,

Vol. 111, 71–90, 2011.

35. Jian, L., G. Xu, G. Yu, J. Song, J. Liang, and M. Chang, "Electromagnetic design and analysis of a novel magnetic-gear-integrated wind power generator using time-stepping finite element method," *Progress In Electromagnetics Research*, Vol. 113, 351–367, 2011.
36. Zhao, W., M. Cheng, R. Cao, and J. Ji, "Experimental comparison of remedial single-channel operations for redundant flux-switching permanent-magnet motor drive," *Progress In Electromagnetics Research*, Vol. 123, 189–204, 2012.
37. Torkaman, H. and E. Afjei, "Comparison of three novel types of two-phase switched reluctance motors using finite element method," *Progress In Electromagnetics Research*, Vol. 125, 151–164, 2012.
38. Torkaman, H. and E. Afjei, "Comparison of three novel types of two-phase switched reluctance motors using finite element method," *Progress In Electromagnetics Research*, Vol. 125, 151–164, 2012.
39. Xu, G., L. Jian, W. Gong, and W. Zhao, "Quantitative comparison of flux-modulated interior permanent magnet machines with distributed windings and concentrated windings," *Progress In Electromagnetics Research*, Vol. 129, 109–123, 2012.
40. Norhisam, M., S. Ridzuan, R. N. Firdaus, C. V. Aravind, H. Wakiwaka, and M. Nirei, "Comparative evaluation on power-speed density of portable permanent magnet generators for agricultural application," *Progress In Electromagnetics Research*, Vol. 129, 345–363, 2012.
41. Release 13.0 documentation for ANSYS, ANSYS Inc., Canonsburg, PA, 2010.
42. Ong, C. M., *Dynamic Simulation of Electric Machinery: Using MATLAB/Simulink*, Prentice Hall PTR, New Jersey, 1998.
43. Hassanpour Isfahani, A. and S. Vaez-Zadeh, "Line start permanent magnet synchronous motors: Challenges and opportunities," *Energy*, Vol. 34, No. 11, 1755–1763, Nov. 2009.